Title

Peripapillary Scleral Bowing Increases with Age and Is Inversely Associated with Peripapillary Choroidal Thickness in Healthy Eyes

Authors

Wang, Ya Xing
Yang, Hongli
Luo, Haomin
et al.

Publication Date

2020-09-01

DOI

10.1016/j.ajo.2020.03.050

Peer reviewed

HHS Public Access

Author manuscript

Am J Ophthalmol. Author manuscript; available in PMC 2022 June 24.

Published in final edited form as:

Am J Ophthalmol. 2020 September ; 217: 91–103. doi:10.1016/j.ajo.2020.03.050.

Peripapillary Scleral Bowing Increases with Age and is Inversely Associated with Peripapillary Choroidal Thickness in Healthy Eyes

Ya Xing Wang, MD[1,2,3],

Hongli Yang, PhD[1,2],

Haomin Luo, MD[1,2,7],

Seung Woo Hong, MD, PhD[1,2,4],

Stuart K Gardiner, PhD[2],

Jin Wook Jeoung, MD, PhD[1,2,6],

Christy Hardin, MA[1,2],

Glen P Sharpe, MSc[5],

Kouros Nouri-Mahdavi, MD, MS[8],

Joseph Caprioli, MD[8],

Shaban Demirel, PhD[2],

Christopher A Girkin, MD[9],

Jeffrey M Liebmann, MD[10],

Christian Y Mardin, MD[11],

Harry A Quigley, MD[12],

Alexander F Scheuerle, MD[13],

Brad Fortune OD, PhD[2],

Balwantray C Chauhan, PhD[5],

Claude F Burgoyne, MD[1,2]

[1]Devers Eye Institute Optic Nerve Head Research Laboratory, Legacy Research Institute, Portland, OR, USA

[2]Devers Eye Institute Discoveries in Sight Research Laboratories, Legacy Research Institute, Portland, OR, USA

[3]Beijing Institute of Ophthalmology, Beijing Tongren Hospital, Beijing Key Laboratory of Ophthalmology and Visual Sciences, Capital Medical University, Beijing, China.

[4]Department of Ophthalmology and Visual Sciences, Medical College, the Catholic University of Korea, Seoul, Korea.

Corresponding Author Claude F. Burgoyne, MD, Optic Nerve Head Research Laboratory, Legacy Research Institute, 1225 NE 2nd Ave Portland, OR 97208-3950, cfburgoyne@deverseye.org.

[5]Department of Ophthalmology and Visual Sciences, Dalhousie University, Halifax, NS, Canada.

[6]Department of Ophthalmology, Seoul National University College of Medicine, Seoul, Korea.

[7]Department of Ophthalmology, Second Xiangya Hospital, Central South University, Hunan, China.

[8]Stein Eye Institute, David Geffen School of Medicine at UCLA, Los Angeles, CA, USA

[9]Department of Ophthalmology, University of Alabama at Birmingham School of Medicine, Birmingham, Alabama, USA

[10]Bernard and Shirlee Brown Glaucoma Research Laboratory, Edward S. Harkness Eye Institute, Department of Ophthalmology, Columbia University Medical Center, New York, USA

[11]Department of Ophthalmology, University of Erlangen-Nuremberg, Erlangen, Germany.

[12]Wilmer Eye Institute, Johns Hopkins University, Baltimore, MD, USA.

[13]Department of Ophthalmology, University of Heidelberg, Heidelberg, Germany.

Abstract

Purpose: To use optical coherence tomography (OCT) to 3D characterize optic nerve head (ONH) peripapillary scleral bowing in non-highly myopic healthy eyes.

Design: Cross-sectional, multicenter study.

Methods: 362 non-highly myopic (+6 diopters (D) > spherical equivalent > −6D) eyes of 362 healthy subjects aging from 20–90 years underwent OCT ONH radial B-scan imaging. Bruch's membrane (BM), BM opening (BMO), anterior scleral canal opening (ASCO) and the peripapillary scleral surface were segmented. BMO and ASCO planes were fit and their centroids, major axes, ovality, area and offset were determined. Peripapillary scleral bowing was characterized by two parameters: *peripapillary scleral slope* (*ppSS)* of three anterior peripapillary scleral segments (0–300, 300–700 and 700–1000 μm from the ASCO centroid); and ASCO depth relative to a peripapillary scleral reference plane *(ASCOD–ppScleral). Peripapillary choroidal thickness (ppCT)* was calculated relative to the ASCO as the minimum distance between the anterior scleral surface and BM.

Results: *ppSS* and *ASCOD-ppScleral* both ranged from slightly inward through profoundly outward in direction. Both parameters increased with age and were independently associated with decreased *ppCT.*

Conclusions: In non-highly myopic healthy eyes outward peripapillary scleral bowing achieved substantial levels, was markedly increased with age and was independently associated with decreased peripapillary choroidal thickness. Our findings provide a normative foundation for characterizing this anatomy in high myopia and glaucoma and in eyes with optic disc tilt, torsion and peripapillary atrophy.

Abstract

We characterized peripapillary scleral bowing in non-highly myopic healthy eyes using two novel parameters - one based on the slope of the peripapillary sclera and the other based on the depth of ASCO relative to a peripapillary reference plane. In 362 non-highly myopic healthy eyes we found

that outward peripapillary scleral bowing achieved substantial levels, was markedly increased with age and was independently associated with decreased peripapillary choroidal thickness. Our findings provide a normative foundation for characterizing this anatomy in high myopia and glaucoma and in eyes with optic disc tilt, torsion and peripapillary atrophy.

Keywords

3D Imaging; Aging; Anterior Scleral Canal Opening; Bruch's Membrane Opening; Glaucoma; Imaging Anatomy; Optic Nerve Head; Optical Coherence Tomography; Sclera; Myopia; Peripapillary Atrophy; Peripapillary Scleral Bowing

Introduction

We use the term "neural canal" to refer to the optic nerve head (ONH) connective tissue pathway that the retinal ganglion cell (RGC) axons pass through on their way to achieve the orbital optic nerve.[1, 2] The neural canal extends from Bruch's membrane opening (BMO) through the anterior and posterior scleral canal openings (Figure 1). We have proposed that the offset of the anterior scleral canal opening (ASCO) relative to BMO, (ASCO/BMO offset) to determine the direction, obliqueness and minimum cross-sectional area of the neural canal.[1] We also hypothesize that temporal displacement of BMO relative to the ASCO and outward bowing of the peripapillary sclera bowing fundamentally underlie the phenotype of the ONH tissues in non-highly myopic and highly myopic eyes, and that both contribute to a given ONH's susceptibility to developing peripapillary atrophy and/or glaucomatous damage at all levels of intraocular pressure, (IOP) including those that are considered statistically normal.

An increase in peripapillary scleral bowing with age was recently reported[3] in 619 elderly (mean age, 60 years) Chinese subjects using a single horizontal B-scan in which a *"peripapillary scleral angle"* was estimated by projecting lines parallel to the nasal and temporal anterior peripapillary scleral surfaces and measuring the angle of their intersection. By the conventions of that study, if those lines intersected in an upright "V" peripapillary scleral bowing was positive (outward) in direction and if the "V" was inverted it was negative (inward) in direction. The elderly eyes in that study predominantly demonstrated outward peripapillary scleral bowing and even within this constrained age range, outward bowing significantly increased with age and was significantly associated with peripapillary choroidal thinning.

The fact that peripapillary scleral bowing increased with age, and was associated with peripapillary choroidal thinning in that study, suggests that peripapillary scleral bowing may mechanistically contribute to the increase in the prevalence of peripapillary atrophy with age[4–8] and in glaucoma.[5, 9, 10] We[11, 12] and others[13–21] have emphasized the biomechanical links between the peripapillary sclera, the dural sheath insertion,[2, 22, 23] the laminar beam insertions and the small penetrating branches of the posterior ciliary arteries that supply the juxta-canalicular choroid and laminar beams.[24] Hayreh demonstrated that this blood supply was preferentially susceptible to acute IOP elevation,[25] and hypothesized that compromise

of this blood supply contributed to a primary vascular insult in glaucoma and the frequent presence of peripapillary choroidal atrophy in aging and glaucoma.[26]

The purpose of the present study was to use OCT imaging to three dimensionally (3D) characterize peripapillary scleral bowing in non-highly myopic healthy eyes using two parameters - one based on the slope of the peripapillary sclera (*peripapillary scleral slope* - (*ppSS*)) and the other based on the depth of ASCO relative to a peripapillary reference plane (*ASCO depth relative to a peripapillary scleral reference plane* (*ASCOD–ppScleral)).* We then determined the association of each parameter with ocular and demographic factors such as age, axial length and peripapillary choroidal thickness.[27]

Methods

Conventions.

We use the term ONH to refer to the tissues that are contained within the scleral canal and those immediately adjacent to it (i.e., the peripapillary sclera, choroid, and retina as well as the immediate retrolaminar optic nerve). In this report we italicize OCT parameters to distinguish the parameters from the morphologic relationships they measure.

Participants.

A total of 362 healthy individuals were recruited from 8 centers (5 in the United States, 2 in Germany and 1 in Canada).[1, 27–29] Among these are 246 self-identified as European Descent, 47 as Hispanic Ethnicity, 47 as African Descent, 19 as Asian Descent, and 3 as Native American Descent participants. Approximately equal numbers of subjects were recruited in each decade group from 20 to 90 years. At the first visit a medical and ophthalmic history was obtained, followed by intraocular pressure (IOP) measurement, anterior segment and external eye examinations, Van Herrick angle assessment, standard Snellen or Early Treatment Diabetic Retinopathy Study (ETDRS) visual acuity, refraction, central keratometry, and axial length assessments. Standard automated perimetry (Humphrey 24–2 Swedish Interactive Thresholding Algorithm, Carl Zeiss Meditec, Dublin, CA) was repeated once if deemed unreliable or outside normal limits. OCT imaging, ophthalmoscopic examination of the posterior pole, and stereophotography were followed by Goldmann applanation tonometry and pachymetry.

All test procedures were performed on both eyes of each participant, but only one eye was randomly selected for analysis. Participants were recruited to represent the ethnic composition of the US population[30] as mandated by the US Food and Drug Administration. The study adhered to the declaration of Helsinki for research involving human participants and was approved by the institutional review board of each participating institution. Each participant provided signed informed consent.

Inclusion criteria included: (1) age between 18 and 90 years, (2) clinically normal eye examination results without clinically significant vitreoretinal or choroidal disease and prior intraocular surgery except cataract or refractive surgery, (3) IOP of 21 mmHg or less, (4) best-corrected visual acuity of 20/40 or better, (5) refractive error within 6 diopters (D) spherical error and 2D astigmatic error, and (6) normal visual field with the glaucoma

hemifield test and mean deviation within normal limits. Subjects were excluded if any of the following were found: (1) history of glaucoma, (2) ONH photographs of insufficient quality, (3) OCT images of insufficient quality (see below), or (4) unreliable visual field results.

OCT Image Acquisition and Segmentation.

The ONH, peripapillary retinal nerve fiber layer and macula were imaged with spectral domain OCT (Spectralis, Heidelberg Engineering GmbH, Heidelberg, Germany, software version Heyex 1.9.10.0). Prior to image acquisition, refractive correction and keratometry values were entered into the system software. The operator then manually identified and marked the fovea in a live B-scan, then centered the imaging field on the ONH, where the 2 BMO points in each of 2 perpendicular ONH radial B-scans were identified. These steps established the eye-specific, fovea-BMO (FoBMO) axis, which was used as the reference for the acquisition of all OCT B-scans (Figure 1).[31–33] The complete ONH imaging pattern consisted of 24 radial B-scans (15° apart with each B-scan containing 768 A-scans) centered on BMO and acquired in EDI mode[34] with an average of 25 repetitions each.

Raw OCT volumes were exported from the device and imported into custom 3D visualization and segmentation software (ATL 3D Suite).[35] ONH and peripapillary landmarks were manually segmented[1, 27, 28] in each radial B-scan and then reconstructed 3-dimensionally (Figure 1). Segmented landmarks included: the internal limiting membrane, posterior surface of the Bruch's membrane/retinal pigment epithelium complex, BMO, neural canal wall, anterior scleral surface, and the ASCO (segmented on each side of the canal by visually projecting the plane of the peripapillary anterior scleral surface through the neural canal wall and marking their intersection).[1, 27, 28] All manual segmentations were performed by trained observers within the Optic Nerve Head Research Laboratory of the Devers Eye Institute.

OCT parameters by ONH morphology.

Quantification of all parameters was performed in MATLAB (Version 9.0.0.341360; The MathWorks, Natick, MA). All left eye data were converted to right eye format. For each eye, separate ellipses and planes were fitted to the 48 segmented BMO and 48 segmented ASCO points, each satisfying a least mean square error restraint. BMO points, ASCO points, and the anterior scleral surface points were interpolated using B-splines (Figure 1). Based on the BMO fitted ellipse, a BMO centroid, area, and ovality index (ellipse major axis /ellipse minor axis) were calculated.[36] An ASCO centroid, area, and ovality index were similarly calculated.

To characterize peripapillary scleral bowing, two OCT parameters, *peripapillary scleral slope (ppSS)* and *ASCO depth relative to a 1700 μm peripapillary scleral reference plane (ASCOD–ppScleral)* were employed. For both parameters, by convention, "inward" peripapillary scleral bowing was defined to be negative in direction and "outward" peripapillary scleral bowing was defined to be positive in direction (Figures 2 and 3). Because positive and negative sectoral values for both parameters cancelled one another when considered globally, sectoral *ppSS* and sectoral *ASCOD-ppScleral* are emphasized.

ppSS.

The anterior peripapillary scleral surface in each B-scan was fitted with a three-segmented linear model implemented with a non-linear curve-fitting function LSQCURVEFIT in Matlab (Version 7.3.0.267, MathWorks, Natick, MA) which minimized the least square error between fitted and raw values. Three peripapillary scleral segments (0–300 μm), (300 to 700 μm), and (700 to 1000 μm), were measured relative to each ASCO point within the ASCO reference plane and projected to the anterior scleral surface (Figure 2). Within each B-scan, the slope sign (direction) for each segment was defined relative to a plane, (parallel to the ASCO reference plane) through its most distal point. For each segment segmental slope was positive (outward bowing) when the proximal segmental point was below the distal segment point and negative (inward bowing) when the proximal segment point was above the distal segment point. Sectoral slope values for each anterior scleral segment were calculated as the average slope value of the four B-scans within each sector. Global *ppSS* values for each segment were calculated as the mean of the 48 B-scan slope values per segment. Slope data were multiplied by 100 for presentation and analysis.

ASCOD–ppScleral.

ASCOD-ppScleral measures the depth of the ASCO relative to a peripheral scleral reference plane (Figure 3) created by fitting a plane to 48 anterior scleral surface points located 1700 μm from the ASCO centroid within each radial B-scan (MATLAB Version 7.3.0.267, MathWorks, Natick, MA). *ASCOD–ppScleral* was determined at each segmented ASCO point as the minimum distance to the peripapillary scleral reference plane (negative when above the plane and positive when below). *ASCOD–pScleral* was defined sectorally as the average depth value of the four ASCO points within each 30^{o} sector and globally as the average value of all 48 ASCO measurement points.

Other OCT Parameters.

In order to assess their associations with the primary OCT parameters of this study, the following previously reported[1, 27–29] parameters were generated as briefly described below.

ASCO/BMO offset magnitude, neural canal direction, neural canal obliqueness and neural canal minimum cross-sectional area (NCMCA).[1]

ASCO/BMO offset magnitude was defined by projecting the ASCO/BMO centroid vector (the vector connecting the BMO and ASCO centroids, also called the neural canal axis vector) to the BMO reference plane and measuring the length of its projection. *Neural canal obliqueness* was defined by the angle between the ASCO/BMO centroid vector and the BMO centroid vector (a vector perpendicular to the BMO plane that passes through the BMO centroid).

Peripapillary choroidal (ppChoroidal) thickness (ppCT).[27]

Global and 30^{o} sectoral *ppCT* measurements were generated as the minimum distance between the anterior scleral surface and Bruch's Membrane at 100, 300, 500, 700, 900 and 1100 microns from the ASCO.

Reproducibility.

Inter-observer segmentation reproducibility was assessed for all parameters within 8 OCT data sets from 8 study eyes independently segmented by 4 operators.

Statistical Analysis.

All statistical analyses were performed with IBM SPSS Statistics (version 24.0, International Business Machines (IBM) Corp., Armonk, NY) and R Statistical Software version 3.1.3 (Foundation for Statistical Computing, Vienna, Austria). Intraclass correlation coefficients (ICC) between observers for each parameter were calculated using a two-way mixed model for agreement.[37] To assess the associations of demographic and ocular variables, as well other OCT parameters with the global *ppSS* and *ASCOD-ppScleral*, univariate and multivariable linear regression models were created as outlined in Supplemental Figure 1. Variables or parameters that achieved a significance of $p < 0.2$ in univariate analyses were entered into the multivariable regression, and variables achieving a significance of $p < 0.05$ and a variance inflation factor of < 5 were considered to be significant.[38]

For sectoral *ppSS* and *ASCOD-ppScleral*, an analysis of variance (ANOVA) using a generalized estimating equation (GEE) model determine whether the parameters varied between sectors, followed by a post-hoc Tukey's test to identify significant pairwise differences. For each variable that was significantly associated with *ppSS* or *ASCOD-ppScleral*, further GEE models were used to assess if the association varied between FoBMO ONH sectors (Supplemental Figure 2). For the parameter *ppSS,* to account for the number of sectors and segments, and therefore the number of comparisons, the model only included variables for which three contiguous sector-segments achieved a significance of $p < 0.05$ and a variance inflation factor of < 5 (12 FoBMO sectors x 3 *ppSS* segments (0–300 μm, 300–700 μm, 700–1000 μm) = 36 sector-segments total). For *ASCOD-ppScleral*, (which was reported in 12 FoBMO sectors), the model required 2 contiguous FoBMO sectors to achieve significance by the same criteria for a variable to be included. We separately identified the subset of sectors (*ASCOD-ppScleral*) or sector-segments (*ppSS*) for which the p-value in the multivariable analyses ($p < 0.05$) achieved significance after Bonferroni correction ($p < 0.00139$, (36 sector-segments) for *ppSS* and $p < 0.00416$, (12 sectors) for *ASCOD-ppScleral*).

Results

Three hundred sixty-two eyes of 362 subjects were studied. Demographic and ocular data overall and by ethnicity have been previously reported [1, 27, 28] and are summarized in Table 1.

ppSS.

Mean global *ppSS (0–300)*, *ppSS (300–700)*, and *ppSS (700–1000)* are reported in Table 2. The distribution of global *ppSS* at each ASCO distance (Figure 4) extended from modestly negative (inward bowing by convention) to substantially positive (outward bowing by convention). Overall and age-stratified sectoral *ppSS* values are reported in Figure 5. Mean sectoral *ppSS (0–300)* differed between sectors ($p<0.0001$, GEE ANOVA), ranging

from 2.23 to 4.35, with the two steepest sectors (temporal and temporal-superior) each significantly steeper than the two flattest sectors (nasal-inferior and inferiornasal) (each comparison $p \leq 0.05$, Tukey's test, Figure 5). Mean sectoral *ppSS (300–700)* also differed between sectors ($p<0.0001$, GEE ANOVA), ranging from 1.32 to 4.24 with the three steepest sectors (temporal, temporal-inferior and inferior-temporal) each steeper than the six flattest sectors (superior-temporal, superior, superior-nasal, nasal-superior, nasal and nasal-inferior) (Figure 5). Finally, mean sectoral *ppSS (700–1000)* also differed between sectors ($p<0.0001$, GEE ANOVA) ranging from 1.57 to 4.33 with the two steepest sectors (inferior and inferior-temporal) each steeper than the six flattest sectors (superior-temporal, superior, superior nasal, nasal-superior, nasal and nasal inferior) (Figure 5).

Global *ppSS* for all three *peripapillary scleral* segments increased with age, (standardized coefficient Beta = 0.24, 0.34 and 0.45, respectively; all $P < 0.001$) (Table 3). More modest effects were also significant for *BMO/ASCO area ratio*, *ASCO ovality, ASCO/BMO offset* and *ppCT* (Table 3). The sectoral effects of age, IOP, *BMO/ASCO area ratio*, *ASCO ovality, ASCO/BMO offset and ppCT* are presented and compared in Figure 6 and Table 3.

ASCOD–ppScleral.

Mean global *ASCOD–ppScleral* and its distribution by age are shown in Table 2, and Figure 4, respectively. Mean sectoral *ASCOD–ppScleral* differed between sectors ($p<0.0001$, GEE ANOVA), ranging from 18.6 to 34.0 μm with the two steepest sectors (temporal-inferior and temporal) each significantly steeper than the five flattest sectors (superior-temporal, superior, superior-nasal, nasal-superior and inferior) ($p \leq 0.05$, Tukey's test; Figure 5). By multivariable analysis, global *ASCOD–ppScleral* substantially increased with age (Beta = 0.38, $P < 0.001$), modestly increased with IOP and ASCO ovality, modestly decreased with *BMO/ASCO area ratio* and was modestly associated with decreasing *ppCT* (Table 3). Significant sectoral effects were present in all 12 sectors for age and *BMO/ASCO area ratio*) and more localized for IOP (temporally), *ASCO ovality* (nasally) and *ppCT*, respectively (Figure 6).

Inter-Observer Reproducibility.

ICC showed moderate to excellent reproducibility for global and sectoral parameters (Supplemental Table 1).

Discussion

This study introduces two new, three-dimensional (3D), OCT parameters to characterize peripapillary scleral bowing, categorized as *ppSS* based on the peripapillary sclera and *ASCOD-ppScleral* based on the depth of ASCO relative to a peripapillary reference plane, in a large cohort of healthy eyes. In so doing it lays a foundation for the incorporation of these ONH morphologic components into OCT-based strategies to clinically phenotype and stage ppScleral bowing[3] and posterior scleral remodeling[39–42] in aging, glaucoma and myopia (Figure 7).[43–49]In healthy eyes both peripapillary scleral bowing parameters reached substantial levels in a subset of eyes, dramatically increased with age and were independently associated with peripapillary choroidal thinning.

Peripapillary scleral bowing increased with age and was significantly associated with peripapillary choroidal thinning in 619 elderly (mean age, 60 years) Chinese subjects using a single horizontal B-scan.[3] Our study replicates both of these findings, extends them to a different ethnic population that spans a much larger age range, and introduces a 3D characterization of peripapillary scleral bowing that includes sectoral measurements of peripapillary scleral slope and ASCO depth relative to a peripapillary scleral reference plane. Our approach will allow peripapillary scleral bowing to be precisely mapped within individual eyes (Figure 7) so as to assess its contribution to ONH susceptibility in future cross-sectional and longitudinal studies.

The fact that peripapillary scleral bowing increased with age and was independently associated with peripapillary choroidal thinning (after accounting for age effects) in both studies suggests that it may mechanistically contribute to the increase in the prevalence of peripapillary atrophy with age[4–8] and in glaucoma.[5, 9, 10] Outward bowing of the peripapillary sclera and peripapillary atrophy are also hallmarks of the clinical appearance of the ONH in high myopia.[13, 50–53] Age and high myopia are two of the most important risk factors for glaucoma at all levels of IOP especially when it occurs at statistically normal levels of IOP.[54–56] Our findings support the broader concept that the presence of peripapillary scleral bowing may increase the susceptibility of the ONH tissues to peripapillary choroidal atrophy and glaucoma in eyes of all ages and axial lengths.[13] Our findings therefore suggest that cross-sectional and longitudinal studies to test these hypotheses may be indicated.[13]

The limitations of this study include the fact that in this paper (and the papers that precede it)[1, 27,28] we identified the ASCO by projecting the immediate peripapillary scleral surface, through the border tissues of Elschnig, to the neural canal boundary (Figure 1). Unlike BMO, which is an anatomically identifiable structure in most non-myopic eyes [57] by histology and by OCT,[36, 58, 59] the ASCO is not an anatomically identifiable structure in either modality. However, while ASCO was estimated in this manner, the inter-operator reproducibility of ASCO area and all related parameters were excellent. The clinical utility of the ONH parameters we report is additionally limited by the fact that automated segmentation of the underlying anatomic landmarks is not yet possible, and manual segmentation by trained observers is required. However, we believe that if the clinical importance of the deep ONH anatomy of this study can be demonstrated, manual segmentations of that anatomy will provide training and testing data sets for the optimization of automated approaches.

Finally, while we acknowledge that the use of manual segmentation limits the immediate clinical application of this work, the segmented anatomy and parameters we have generated are also a strength of this study. Unsupervised deep learning algorithms[60, 61] which work with raw (unsegmented) OCT images may eventually incorporate the anatomy of this study into strategies for detecting glaucoma and its progression without segmenting any ONH anatomic targets. However, supervised machine learning algorithms[62, 63] which require segmented anatomy and/or parameterization may also be required to inform our understanding of disease staging and mechanisms. Structurally distinguishing and staging the effects of aging, glaucoma and myopia on the ONH tissues is important because it may

provide insight into their respective underlying pathophysiologic mechanisms and inform future therapeutic interventions. We believe that manually segmented anatomy will be a required component of efforts to move the field toward disease staging and automated interpretations of OCT anatomy.

In summary, we developed a 3D, OCT-based strategy to clinically characterize ppScleral bowing and used it to study non-highly myopic eyes that included up to −6 D of spherical equivalent refractive error. We found that ppScleral bowing can be substantial in non-highly myopic healthy eyes, increased dramatically with age and was independently associated with peripapillary choroidal thinning. Our OCT parameters provide a foundation for cross-sectional and longitudinal studies of this anatomy in aging, glaucoma and high myopia and in eyes with optic disc tilt, torsion and peripapillary atrophy.

Supplementary Material

Refer to Web version on PubMed Central for supplementary material.

Acknowledgements/Disclosure

a. Funding/ Support:

NIH/NEI R01-EY02128; CIHR-PJT-159564; Legacy Good Samaritan Foundation; Heidelberg Engineering, GmbH, Heidelberg, Germany.

b. Financial Disclosure:

YX. Wang: None; H. Yang: None; H. Luo: None; SW. Hong: None; S. Gardiner: Nonfinancial support - Heidelberg Engineering. J.W. Jeoung: None; C. Hardin: None; G. Sharpe: None; K. NourI-Mahdavi: Heidelberg Engineering (R); J. Caprioli: None. S. Demirel: Financial support - Legacy Good Samaritan Foundation, Carl Zeiss Meditec, Heidelberg Engineering, NIH/NEI R01-EY-019674. C. A. Girkin: Financial support - Heidelberg Engineering. J. M. Liebmann: Financial support - Carl Zeiss Meditec, Topcon, Inc, Alcon Laboratories, Allergan, Inc, Diopsys Corporation, Glaukos Corporation, Heidelberg Engineering, Merz Pharmaceutical, Inc, Optovue, Inc, Quark Pharmaceuticals, Inc, SOLX, Inc. C. Y. Mardin; Financial support - Heidelberg Engineering. H. A. Quigley: Financial support - Heidelberg Engineering. A. F. Scheuerle: Financial support - Heidelberg Engineering. B. Fortune: Financial support - Legacy Good Samaritan Foundation, Inotek Pharmaceuticals. B. C. Chauhan: Financial support - Heidelberg Engineering. C. F. Burgoyne: Financial support - NIH/NEI R01-EY021281, Legacy Good Samaritan Foundation, Heidelberg Engineering.

The above listed sponsors/funding organizations had no role in the design, conduct, analysis or reporting of this research.

c. Other Acknowledgments

Drs Ya Xing Wang and Hongli Yang contributed equally to this work.

Presented in part at the Association for Research in Vision and Ophthalmology Annual Meeting. May 2019, Vancouver, Canada

Abbreviations/Acronyms:

ASCO	anterior sclera canal opening
ASCOD-ppScleral	ASCO Depth relative to a peripapillary scleral reference plane
BMO	Bruch’s membrane opening

FoBMO	Fovea-BMO
IOP	intraocular pressure
OCT	optical coherence tomography
ONH	optic nerve head
ppCT	peripapillary choroidal thickness
SD	standard deviation

References

1. Hong S, Yang H, Gardiner SK, et al. OCT-Detected Optic Nerve Head Neural Canal Direction, Obliqueness and Minimum Cross-Sectional Area in Healthy Eyes. AJO 2019;208:185–205.
2. Downs JC, Yang H, Girkin C, et al. Three-dimensional histomorphometry of the normal and early glaucomatous monkey optic nerve head: neural canal and subarachnoid space architecture. IOVS 2007;48;7:3195–208.
3. Tun TA, Wang X, Baskaran M, et al. Variation of Peripapillary Scleral Shape With Age. IOVS 2019;60;10:3275–3282.
4. Burgoyne CF, Downs JC. Premise and prediction-how optic nerve head biomechanics underlies the susceptibility and clinical behavior of the aged optic nerve head. J Glaucoma 2008;17;4:318–28. [PubMed: 18552618]
5. Jonas JB, Fernandez MC, Naumann GO. Parapapillary atrophy and retinal vessel diameter in nonglaucomatous optic nerve damage. IOVS 1991;32;11:2942–7.
6. Wang Y, Xu L, Zhang L, Yang H, Ma Y, Jonas JB. Peripapillary atrophy in elderly Chinese in rural and urban Beijing. Eye (Lond) 2008;22;2:261–6. [PubMed: 17001322]
7. Rockwood EJ, Anderson DR. Acquired peripapillary changes and progression in glaucoma. Graefes Arch Clin Exp Ophthalmol 1988;226;6:510–5. [PubMed: 3209077]
8. Zhang Q, Wang YX, Wei WB, Xu L, Jonas JB. Parapapillary Beta Zone and Gamma Zone in a Healthy Population: The Beijing Eye Study 2011. IOVS 2018;59;8:3320–3329.
9. Jonas JB. Clinical implications of peripapillary atrophy in glaucoma. Curr Opin Ophthalmol 2005;16;2:84–8. [PubMed: 15744137]
10. Buus DR, Anderson DR. Peripapillary crescents and halos in normal-tension glaucoma and ocular hypertension. Ophthalmology 1989;96;1:16–9. [PubMed: 2919047]
11. Burgoyne CF, Downs JC, Bellezza AJ, Suh JK, Hart RT. The optic nerve head as a biomechanical structure: a new paradigm for understanding the role of IOP-related stress and strain in the pathophysiology of glaucomatous optic nerve head damage. Prog Retin Eye Res 2005;24;1:39–73. [PubMed: 15555526]
12. Burgoyne CF. A biomechanical paradigm for axonal insult within the optic nerve head in aging and glaucoma. Exp Eye Res 2011;93;2:120–32. [PubMed: 20849846]
13. Kim EK, Park H-YL, Park CK. Posterior scleral deformations around optic disc are associated with visual field damage in open-angle glaucoma patients with myopia. PLOS ONE 2019;14;3:e0213714. [PubMed: 30875403]
14. Chen JY, Le A, De Andrade LM, Goseki T, Demer JL. Compression of the Choroid by Horizontal Duction. IOVS 2019;60;13:4285–4291.
15. Suh SY, Le A, Shin A, Park J, Demer JL. Progressive Deformation of the Optic Nerve Head and Peripapillary Structures by Graded Horizontal Duction. IOVS 2017;58;12:5015–5021.
16. Langham M The temporal relation between intraocular pressure and loss of vision in chronic simple glaucoma. Glaucoma 1980;2;4:427–435.
17. Pijanka JK, Coudrillier B, Ziegler K, et al. Quantitative mapping of collagen fiber orientation in non-glaucoma and glaucoma posterior human sclerae. IOVS 2012;53;9:5258–70.

18. Coudrillier B, Pijanka J, Jefferys J, et al. Collagen structure and mechanical properties of the human sclera: analysis for the effects of age. J Biomech Eng 2015;137;4:041006. [PubMed: 25531905]
19. Hernandez MR, Luo XX, Igoe F, Neufeld AH. Extracellular matrix of the human lamina cribrosa. AJO 1987;104;6:567–76.
20. Sigal IA, Flanagan JG, Tertinegg I, Ethier CR. Finite element modeling of optic nerve head biomechanics. Invest Ophthalmol Vis Sci 2004;45;12:4378–87. [PubMed: 15557446]
21. Sigal IA, Yang H, Roberts MD, et al. IOP-induced lamina cribrosa deformation and scleral canal expansion: independent or related? IOVS 2011;52;12:9023–32.
22. Burgoyne CF, Downs JC, Bellezza AJ, Hart RT. Three-dimensional reconstruction of normal and early glaucoma monkey optic nerve head connective tissues. IOVS 2004;45;12:4388–99.
23. Yang H, Downs JC, Bellezza A, Thompson H, Burgoyne CF. 3-D histomorphometry of the normal and early glaucomatous monkey optic nerve head: prelaminar neural tissues and cupping. IOVS 2007;48;11:5068–84.
24. Sugiyama K, Cioffi GA, Bacon DR, Van Buskirk EM. Optic nerve and peripapillary choroidal microvasculature in the primate. J Glaucoma 1994;3 Suppl 1;3:S45–54. [PubMed: 19920587]
25. Hayreh SS, Revie IH, Edwards J. Vasogenic origin of visual field defects and optic nerve changes in glaucoma. BJO 1970;54;7:461–72.
26. Hayreh SS. Blood supply of the optic nerve head and its role in optic atrophy, glaucoma, and oedema of the optic disc. BJO 1969;53;11:721–48.
27. Yang H, Luo H, Gardiner SK, et al. Factors Influencing Optical Coherence Tomography Peripapillary Choroidal Thickness: A Multicenter Study. IOVS 2019;60;2:795–806.
28. Luo H, Yang H, Gardiner SK, et al. Factors Influencing Central Lamina Cribrosa Depth: A Multicenter Study. IOVS 2018;59;6:2357–2370.
29. Chauhan BC, Danthurebandara VM, Sharpe GP, et al. Bruch's Membrane Opening Minimum Rim Width and Retinal Nerve Fiber Layer Thickness in a Normal White Population: A Multicenter Study. Ophthalmology 2015;122;9:1786–94. [PubMed: 26198806]
30. Mullin JF. Statistical Abstract of the United States: 2012. In: Branch SC, editor, 2012:940.
31. Burgoyne C The morphological difference between glaucoma and other optic neuropathies. J Neuroophthalmol 2015;35 Suppl 1:S8–S21. [PubMed: 26274837]
32. Chauhan BC, Burgoyne CF. From clinical examination of the optic disc to clinical assessment of the optic nerve head: a paradigm change. AJO 2013;156;2:218–227 e2.
33. He L, Ren R, Yang H, et al. Anatomic vs. acquired image frame discordance in spectral domain optical coherence tomography minimum rim measurements. PLoS One 2014;9;3:e92225. [PubMed: 24643069]
34. Spaide RF, Koizumi H, Pozzoni MC. Enhanced depth imaging spectral-domain optical coherence tomography. AJO 2008;146;4:496–500.
35. Fortune B, Reynaud J, Hardin C, Wang L, Sigal IA, Burgoyne CF. Experimental Glaucoma Causes Optic Nerve Head Neural Rim Tissue Compression: A Potentially Important Mechanism of Axon Injury. IOVS 2016;57;10:4403–11.
36. Strouthidis NG, Yang H, Fortune B, Downs JC, Burgoyne CF. Detection of optic nerve head neural canal opening within histomorphometric and spectral domain optical coherence tomography data sets. IOVS 2009;50;1:214–23.
37. Koo T, Li MY. Abstracts of the Scientific Sessions from the WFC'S 12th Biennial Congress Proceedings, Durban, South Africa, April 10–13, 2013. Journal of Chiropractic Medicine 2013;12;2:92–142. [PubMed: 24294151]
38. Craney TASJ. Model-dependent variance inflation factor cutoff values. Quality Engineering. 2002 Mar 25;14(3):391–403., 2002.
39. Kim YC, Jung KI, Park HL, Park CK. Three-Dimensional Evaluation of Posterior Pole and Optic Nerve Head in Myopes with Glaucoma. Sci Rep 2017;7;1:18001. [PubMed: 29269862]
40. Kim YC, Jung Y, Park HL, Park CK. The Location of the Deepest Point of the Eyeball Determines the Optic Disc Configuration. Sci Rep 2017;7;1:5881. [PubMed: 28725046]

41. Kim YC, Moon JS, Park HL, Park CK. Three Dimensional Evaluation of Posterior Pole and Optic Nerve Head in Tilted Disc. Sci Rep 2018;8;1:1121. [PubMed: 29348471]
42. Moriyama M, Ohno-Matsui K, Hayashi K, et al. Topographic analyses of shape of eyes with pathologic myopia by high-resolution three-dimensional magnetic resonance imaging. Ophthalmology 2011;118;8:1626–37. [PubMed: 21529960]
43. Witmer MT, Margo CE, Drucker M. Tilted optic disks. Surv Ophthalmol 2010;55;5:403–28. [PubMed: 20621322]
44. Lee KM, Lee EJ, Kim TW. Lamina cribrosa configuration in tilted optic discs with different tilt axes: a new hypothesis regarding optic disc tilt and torsion. IOVS 2015;56;5:2958–67.
45. Choi JA, Park HY, Shin HY, Park CK. Optic disc tilt direction determines the location of initial glaucomatous damage. IOVS 2014;55;8:4991–8.
46. Kim TW, Kim M, Weinreb RN, Woo SJ, Park KH, Hwang JM. Optic disc change with incipient myopia of childhood. Ophthalmology 2012;119;1:21–6 e1–3. [PubMed: 21978594]
47. Sung MS, Kang YS, Heo H, Park SW. Characteristics of Optic Disc Rotation in Myopic Eyes. Ophthalmology 2016;123;2:400–7. [PubMed: 26606868]
48. Sung MS, Kang YS, Heo H, Park SW. Optic Disc Rotation as a Clue for Predicting Visual Field Progression in Myopic Normal-Tension Glaucoma. Ophthalmology 2016;123;7:1484–93. [PubMed: 27157844]
49. Marsh-Tootle WL, Harb E, Hou W, et al. Optic Nerve Tilt, Crescent, Ovality, and Torsion in a Multi-Ethnic Cohort of Young Adults With and Without Myopia. IOVS 2017;58;7:3158–3171.
50. Curtin BJ, Iwamoto T, Renaldo DP. Normal and Staphylomatous Sclera of High Myopia: An Electron Microscopic Study. Archives of Ophthalmology 1979;97;5:912–915. [PubMed: 444126]
51. Ohno-Matsui K, Jonas JB. Posterior staphyloma in pathologic myopia. Prog Retin Eye Res 2019;70:99–109. [PubMed: 30537538]
52. Jonas JB, Gusek GC, Naumann GO. Optic disk morphometry in high myopia. Graefes Arch Clin Exp Ophthalmol 1988;226;6:587–90. [PubMed: 3209086]
53. Xu L, Li Y, Wang S, Wang Y, Wang Y, Jonas JB. Characteristics of highly myopic eyes: the Beijing Eye Study. Ophthalmology 2007;114;1:121–6. [PubMed: 17070594]
54. Marcus MW, de Vries MM, Junoy Montolio FG, Jansonius NM. Myopia as a risk factor for open-angle glaucoma: a systematic review and meta-analysis. Ophthalmology 2011;118;10:1989–1994 e2. [PubMed: 21684603]
55. Leske MC, Connell AM, Wu SY, Hyman LG, Schachat AP. Risk factors for open-angle glaucoma. The Barbados Eye Study. Arch Ophthalmol 1995;113;7:918–24. [PubMed: 7605285]
56. Drance S, Anderson DR, Schulzer M. Risk factors for progression of visual field abnormalities in normal-tension glaucoma. AJO 2001;131;6:699–708.
57. Strouthidis NG, Yang H, Downs JC, Burgoyne CF. Comparison of clinical and three-dimensional histomorphometric optic disc margin anatomy. IOVS 2009;50;5:2165–74.
58. Strouthidis NG, Yang H, Reynaud JF, et al. Comparison of clinical and spectral domain optical coherence tomography optic disc margin anatomy. IOVS 2009;50;10:4709–18.
59. Strouthidis NG, Grimm J, Williams GA, Cull GA, Wilson DJ, Burgoyne CF. A comparison of optic nerve head morphology viewed by spectral domain optical coherence tomography and by serial histology. IOVS 2010;51;3:1464–74.
60. Christopher M, Belghith A, Weinreb RN, et al. Retinal Nerve Fiber Layer Features Identified by Unsupervised Machine Learning on Optical Coherence Tomography Scans Predict Glaucoma Progression. IOVS 2018;59;7:2748–2756.
61. Maetschke S, Antony B, Ishikawa H, Wollstein G, Schuman J, Garnavi R. A feature agnostic approach for glaucoma detection in OCT volumes. PLoS One 2019;14;7:e0219126. [PubMed: 31260494]
62. Song Y, Ishikawa H, Wu M, et al. Clinical Prediction Performance of Glaucoma Progression Using a 2-Dimensional Continuous-Time Hidden Markov Model with Structural and Functional Measurements. Ophthalmology 2018;125;9:1354–1361. [PubMed: 29571832]

63. Wang P, Shen J, Chang R, et al. Machine Learning Models for Diagnosing Glaucoma from Retinal Nerve Fiber Layer Thickness Maps. Ophthalmology Glaucoma 2019;2;6:422–428. [PubMed: 32672575]

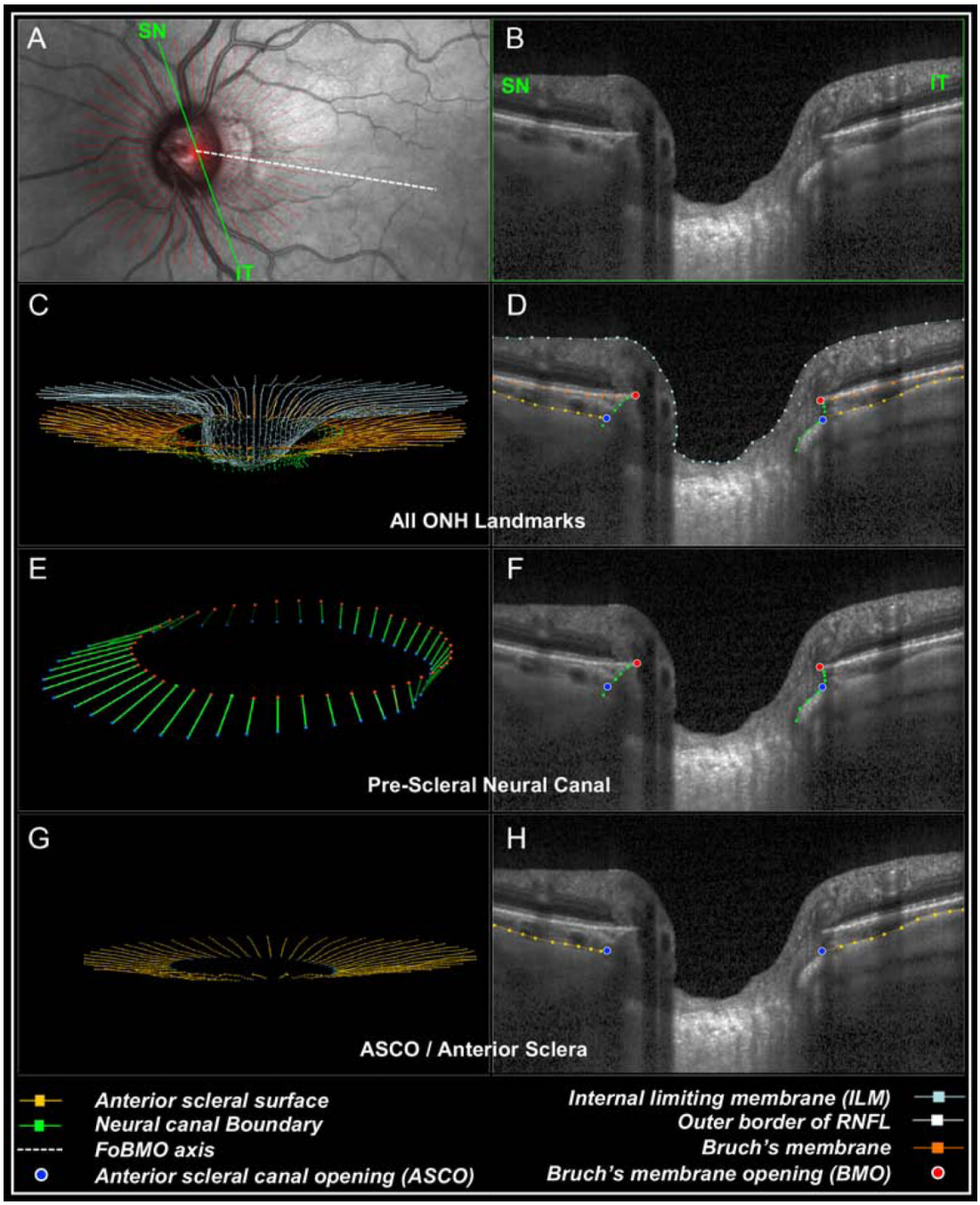

Figure 1. OCT Anatomic Landmarks.

(A) A 24-radial B-scan optical coherence tomography (OCT) data set is shown (red lines) relative to the fovea to BMO centroid (FoBMO) axis (white dotted line). The single green line depicts the representative B-scan shown in **(B)** superior-nasal **(SN)** left and inferior-temporal **(IT)** right. **(C)** The 3D point cloud of all segmented OCT landmark points which are segmented within the Panel B B-scan in **(D)**. **(E)** The pre-scleral neural canal point cloud extends from Bruch's Membrane opening (BMO), along the neural canal boundary to the anterior scleral canal opening (ASCO) as shown within an individual B-scan in **(F). (G)**

The ASCO (blue dots) and anterior scleral canal surface (yellow squares) point cloud which is shown within an individual B-scan in Panel **(H)**. See the Methods section for a detailed description of this anatomy and its segmentation.

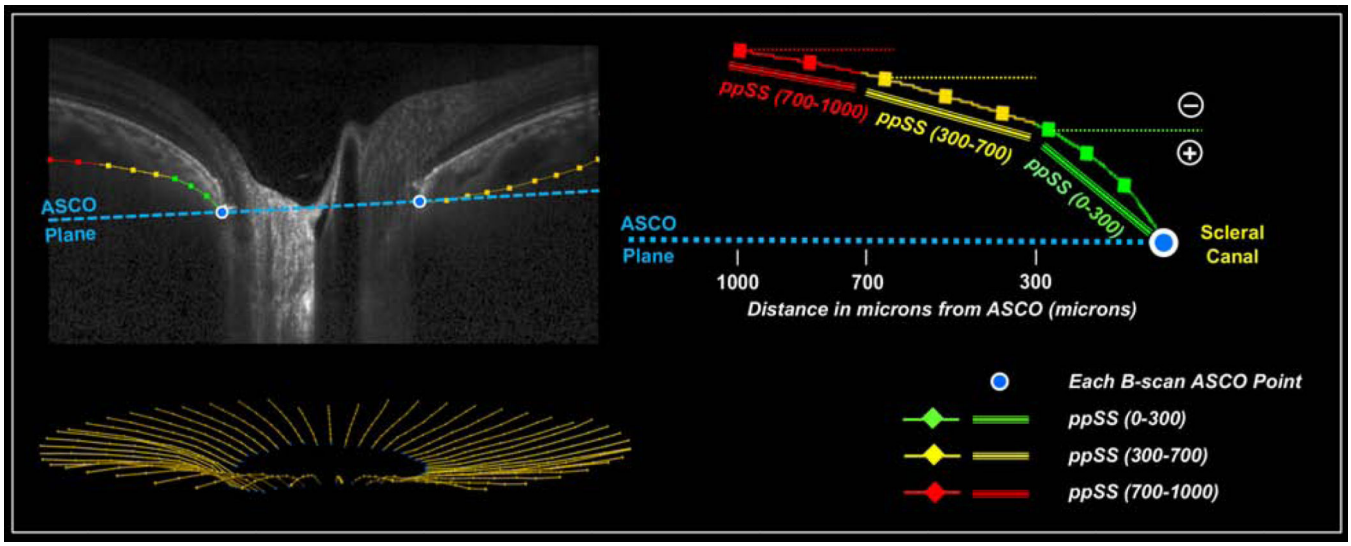

Figure 2. ***Peripapillary scleral slope (ppSS)*** **measured in three anterior ppScleral segments (relative to the distal position of each segment) within each B-scan.**

The peripapillary anterior sclera surface was fitted using a trilinear model and *ppSS* was calculated for three juxta-canalicular anterior scleral segments (*0–300 microns*), (*300 to 700 microns*) and (*700 to 1000 microns*) measured relative to the anterior scleral canal opening (ASCO) within the ASCO reference plane after projection of these measurement points to the anterior scleral surface. Within each B-scan, the slope direction for each anterior scleral segment was determined by the position of its proximal measurement point relative to its distal measurement point. By convention, “inward” peripapillary scleral bowing was defined to be present when the proximal end of a segment was “above” the distal end and its sign was defined to be negative (−). “Outward” peripapillary scleral bowing was defined to be present when the proximal end of a segment was “below” its distal end and its sign was defined to be positive (+). *ppSS* was multiplied by 100 for presentation and analysis. Ǹote that since slope is unitless, *ppSS* is a unitless parameter.

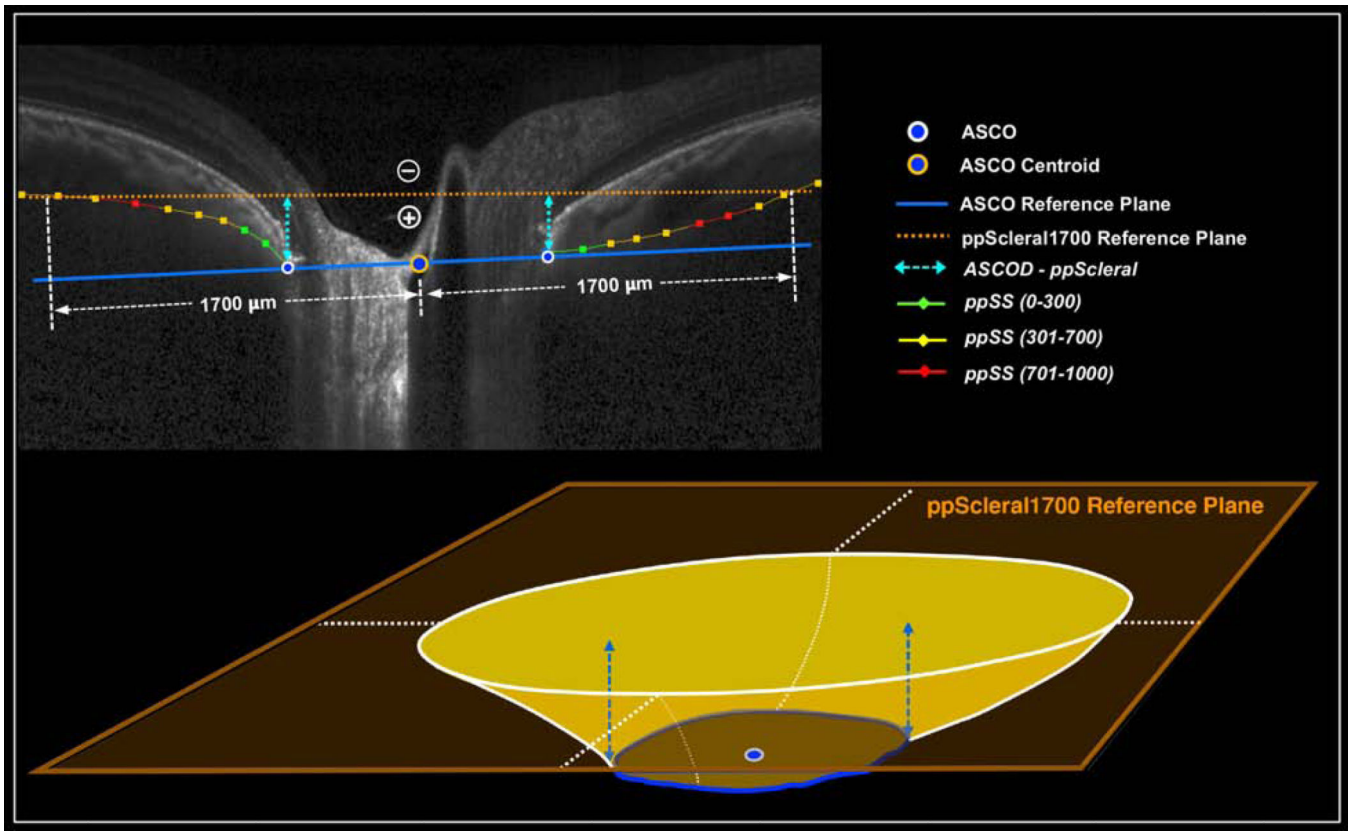

Figure 3. ASCO Depth relative to a 1700 µm peripapillary scleral reference plane *(ASCOD–pScleral)* in 2D (above) and in 3D (below).

A 1700 µm peripapillary scleral reference plane was defined by the plane that best fit the anterior scleral surface points at a distance 1700 µm away from the ASCO centroid (measured within the ASCO reference plane). ASCO depth was defined at each ASCO point as the minimum distance to the pScleral reference plane (negative **(−)** when above the plane and positive **(+)** when below). Global *ASCOD-ppScleral* was defined to be the average of the 48 individual ASCO point depth values. Sectoral *ASCOD-ppScleral* was calculated as the average depth value of the four ASCO points within each sector, (24 radial B-scans, each containing 2 ASCO points, yield 48 ASCO measurement points distributed over twelve 30º FoBMO sectors).

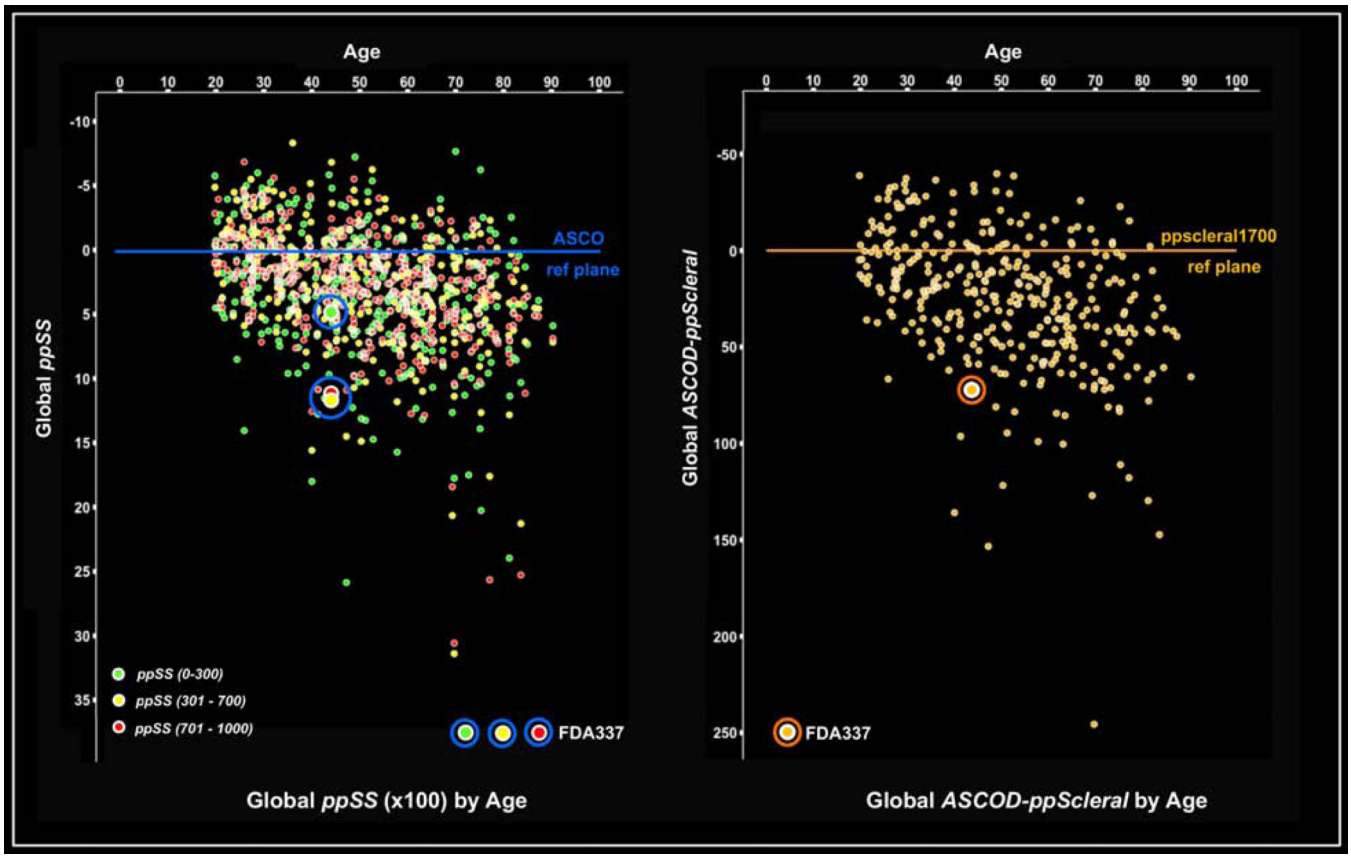

Figure 4. Distribution of global *peripapillary scleral slope (ppSS)* (for each ASCO segment) (left) and global *ASCOD-ppScleral* (right) by age.

For both parameters, by convention, “inward” peripapillary scleral bowing is defined to be negative (upward) in direction and “outward” peripapillary scleral bowing is defined to be positive (downward) in direction (see Methods and Figures 4 and 5). **(Left)** Global data for each *ppSS* segment (0300), (300–700) and (700–1000) (color-coded) for each study eye are plotted. **(Right)** A single global *ASCOD-ppScleral* value is plotted for each study eye. For both parameters, the data for the representative study eye shown in Figure 7, (FDA337), is highlighted.

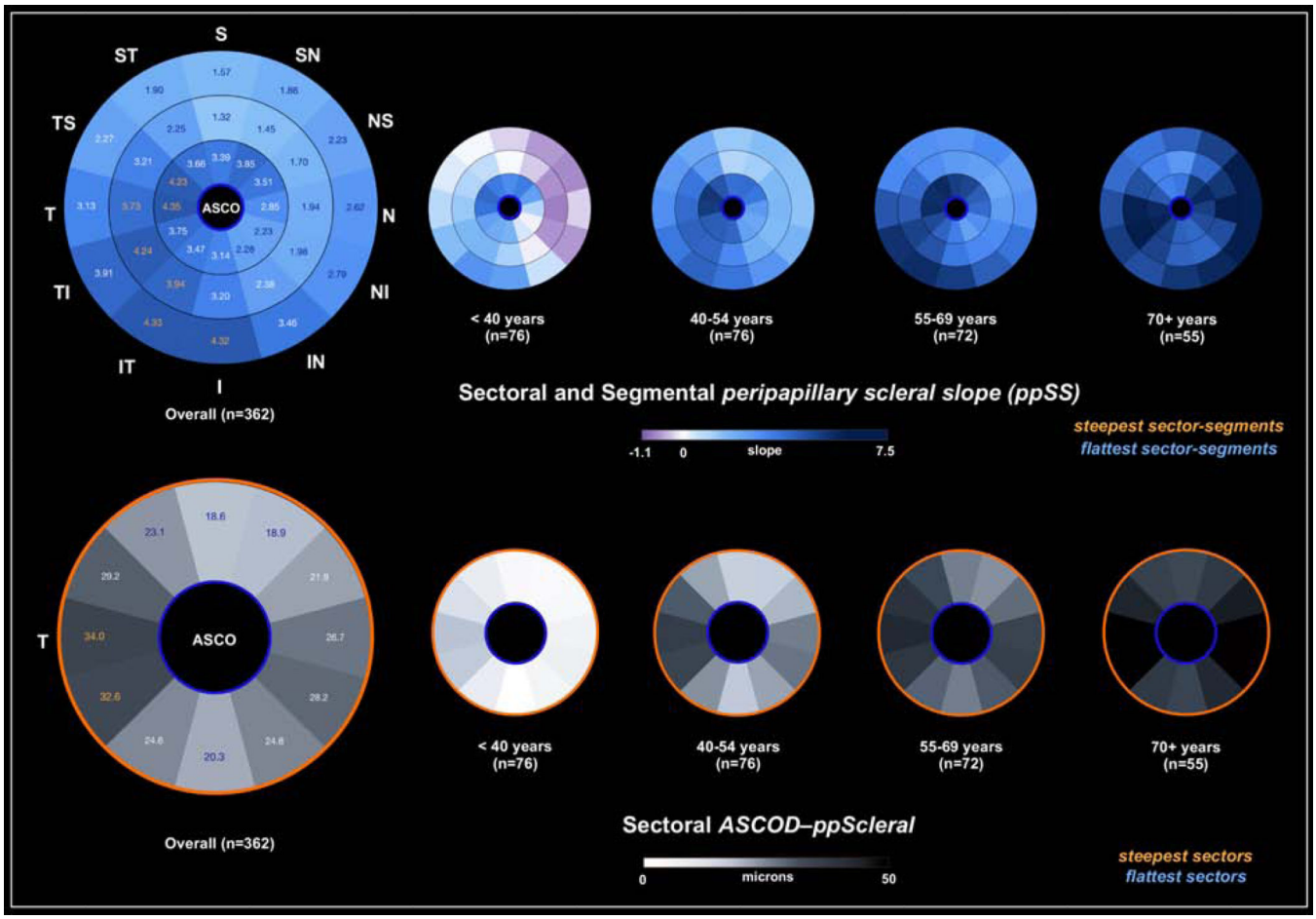

Figure 5. Peripapillary scleral bowing as characterized by sectoral peripapillary scleral slope (ppSS) (above) and sectoral*ASCO depth relative to a peripapillary Scleral Reference Plane (ASCOD-ppScleral)* (below).

Data are shown overall and by age group. The upper *ppSS* plots depict *ppSS* (0–300) segment data (inner ring), *ppSS* (300–700) segment data (middle ring) and *ppSS* (700–1000) segment data (outer ring). In both panels the inner blue ring signifies that data are relative to the ASCO. In the lower panel, the *ASCOD-ppScleral* data are surrounded by a mustard colored outline to convey that they are measurements relative to the peripapillary scleral reference plane (see Figure 3). All data are reported in right eye orientation. Within each ppSS segment and for *ASCOD-ppScleral* the two (or three) steepest sectors (orange fonts) that were each significantly steeper ($p < 0.05$, Tukey test) than the two, three, five or 6 flattest sectors (white underline – the number differing by parameter) are shown. The twelve 30^{O} FoBMO sectors are named as follows: S: superior; SN: superiornasal; NS: nasal-superior; N: nasal; NI: nasal-inferior; I: inferior; IT: inferior-temporal; TI: temporal-inferior; T: temporal; TS: temporal-superior; ST: superior-temporal.

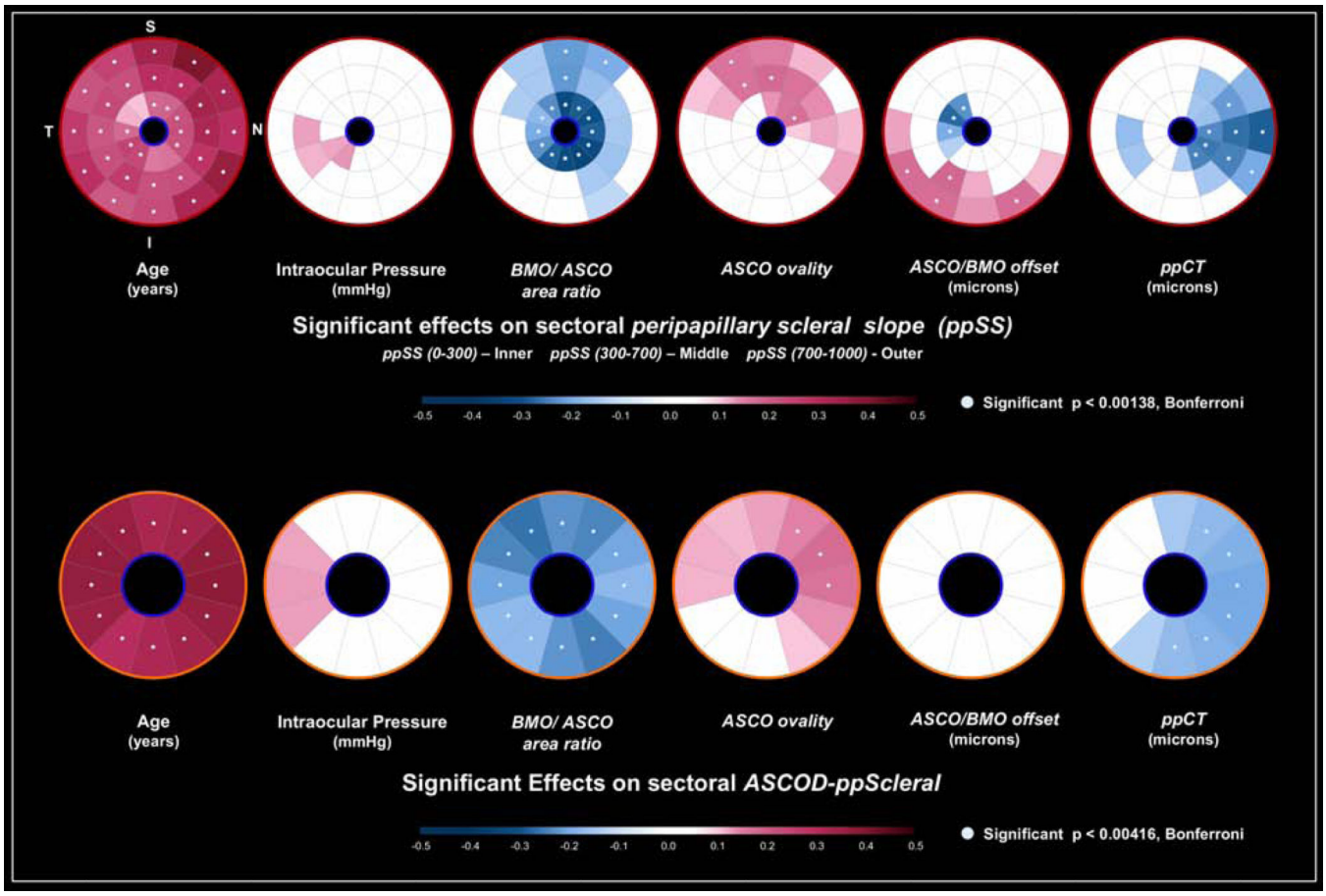

Figure 6. Significant sectoral demographic, ocular and OCT parameter associations with the OCT peripapillary scleral bowing parameters by multivariable analysis.

The strength of a linear relationship between each bowing parameter, (*peripapillary scleral slope* (*ppSS*) above and *ASCOD-ppScleral*, below) and each variable (age, axial length, intraocular pressure, *BMO/ASCO area ratio*, *ASCO ovality*, and *ASCO/BMO offset)* is depicted by the standardized regression coefficients for those sectors that achieved significance ($p \leq 0.05$, multivariable analysis, see Methods and Supplemental Figure 2). The color pink stands for a positive association and blue for a negative association. Because of the number of comparisons and to enhance clinical relevance, we required that each significant variable to have achieved statistical significance within the multivariable analysis in at least two continuous sectors for *ASCOD-ppScleral* (12 sectors) or 3 contiguous sector-segments for *ppSS* (36 sector-segments). Thus single sectoral associations are not reported. All data are reported in right eye orientation (upper left). We then separately identified the subset of sectors (*ASCOD-ppScleral*) or FoBMO sector-segments (*ppSS*) that were significant within the multivariable analyses ($p < 0.05$) with p values that also achieved significance after Bonferroni correction ($p < 0.00139$, (36 sector-segments), *ppSS* and $p < 0.00416$, (12 sectors) *ASCOD-ppScleral*) (white overlaid dots).

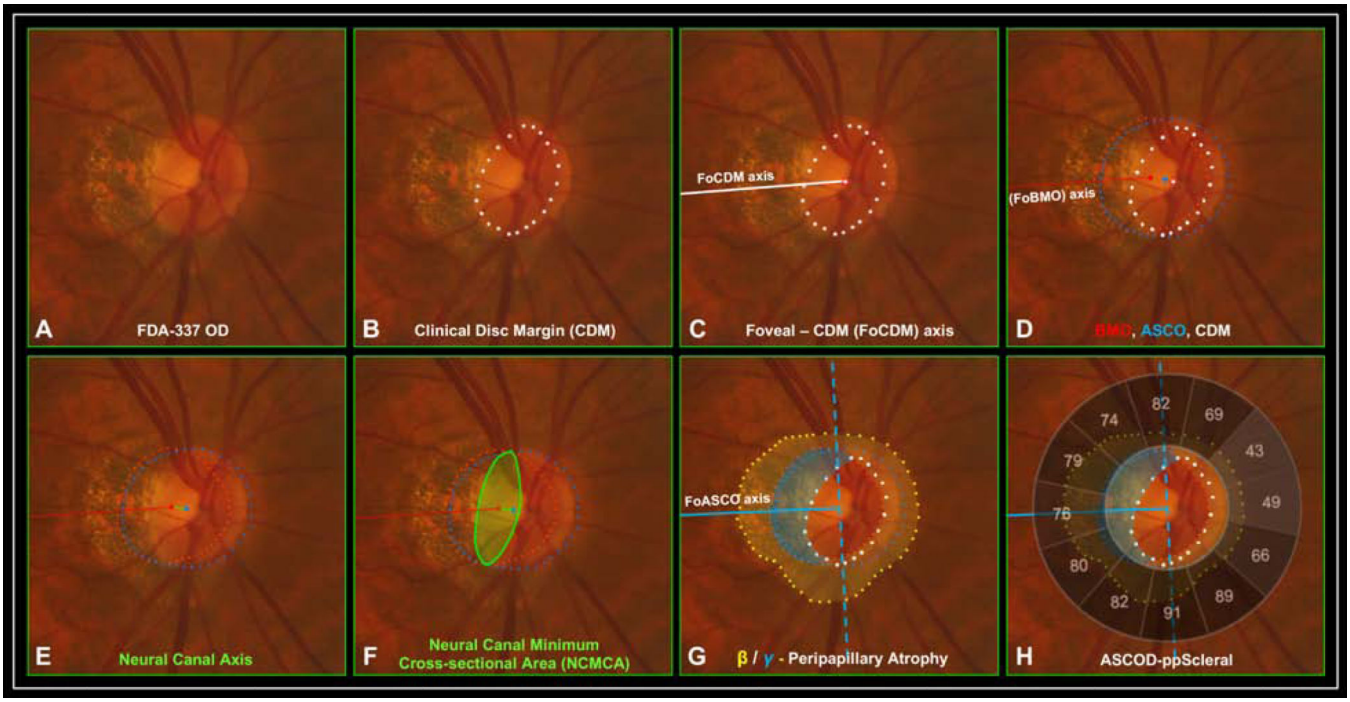

Figure 7. We predict that optic nerve head (ONH) neural canal [1] and peripapillary scleral anatomy contribute to the clinical susceptibility of the ONH tissues to aging, peripapillary atrophy, glaucoma and myopia and that OCT characterization of this anatomy will be required for these contributions to be identified.

(A) Right eye of FDA-337 (axial length: 25.10 mm; spherical equivalent: −5.5 diopter). **(B)** Clinical disc margin **(CDM)** defined by the inner-most hyper-reflective border of the ONH. **(C)** The fovea to CDM centroid **(FoCDM)** axis. **(D)** The CDM, Bruch's membrane opening **(BMO)**, the anterior scleral canal opening **(ASCO)** and the Fovea to BMO centroid (FoBMO) axis projected onto the BMO plane. **(E)** The neural canal axis defined by the vector connecting the BMO and ASCO centroids shown relative to the FoBMO axis for reference. **(F)** The *neural canal minimum cross-sectional area* ***(NCMCA)*** (as defined in a previous publication)[1] is smaller and more elliptical than the CDM, BMO and the ASCO. **(G)** Beta (**β**) and gamma (**γ**) peripapillary atrophy relative to the Fovea to ASCO centroid **(FoASCO)** axis. **(H)** Peripapillary scleral bowing quantified by ***ASCOD-ppScleral*** (grey-scale sectors depict the percentile of the healthy eye distribution (in white)). Cross-sectional and longitudinal studies to determine whether increases in peripapillary scleral bowing underlie the increases in peripapillary atrophy seen in aging, glaucoma and myopia are required.

Table 1.

Demographic and ocular characteristics of the study participants.

	All Subjects n=362	European Descent n=248	Hispanic Descent n=47	African Descent n=47	Asian/Native American Descent [1] n=22	ANOVA or Chi-Square test [2]
Female Gender *n (%)*	202 (56%)	137 (56%)	30 (64%)	22 (47%)	13 (59%)	0.41
Left Eye *n (%)*	181 (50%)	123 (51%)	25 (51%)	25 (53%)	9 (41%)	0.83
Age *(year)* mean (SD)	50.6 (17.5)	52.2 (18.3)	45.3 ± 14.1	49.4 ± 14.8	47.3 ±19.3	0.06
Axial Length *(mm)* mean (SD)	23.7 (1.0)	23.7 (0.9)	23.9 (1.0)	23.8 (1.0)	24.1 (1.1)	0.18
IOP *(mmHg)* mean (SD)	15.0 (3.0)	14.6 (2.7)	14.3 (2.7)	14.9 (2.7)	14.0 (2.5)	0.49
CCT *(μm)* mean (SD)	555 (33)	555 (35)	556 (26)	546 (29)	573 (22)	**0.012**
SE *(diopter)* mean (SD)	−0.47 (1.8)	−0.3 (1.7)	−0.4 (1.9)	−0.8 (1.8)	−1.93 (2.1)	**<0.001**

Table 2.

***Global* peripapillary scleral bowing parameters overall.**

Note that since slope is unitless *ppSS* is a unitless parameter. Note also that *ppSS* is measured between four points measured from the ASCO: the ASCO (0), 300 μm (300), 700 μm (700) and 1000 μm (1000).

Peripapillary Scleral Bowing		Mean (SD)	Range
ppSS	*ppSS (0–300)*	3.4 (4.8)	−7.7, 25.9
	ppSS (300–700)	2.6 (4.4)	−8.3, 31.4
	ppSS (700–1000)	2.9 (4.3)	−6.8, 30.6
ASCOD-ppScleral *(μm)*		25.2 (35.2)	−39.8, 245.6

ppSS: peripapillary scleral slope; ***ASCOD –ppScleral***: ASCO Depth relative to a peripapillary scleral reference plane; **SD**: standard deviation.

Table 3.

Multivariable analysis of demographic, ocular and OCT parameter associations with global OCT peripapillary scleral bowing parameters by linear regression and the significance of sectoral effects on each parameter by general estimation equation (GEE).

		Age	IOP	BMO/ASCO Area Ratio	ASCO Ovality	ASCO/BMO Offset	ppCT
ppSS (0–300)	[1] **Significance of Coefficient**	**<0.001**	/	**<0.001**	**0.040**	**0.023**	**0.001**
	[1] **Standardized Coefficient**	0.24	/	−0.35	0.10	−0.12	−0.20
	[2] **Significance of Sectoral Effect**	**0.028**	/	0.230	**0.010**	**<0.001**	**0.038**
ppSS (300–700)	[1] **Significance of Coefficient**	**<0.001**	/	**0.006**	**0.005**	/	**0.002**
	[1] **Standardized Coefficient**	0.34	/	−0.15	0.15	/	−0.18
	[2] **Significance of Sectoral Effect**	**<0.001**	/	**<0.001**	0.100	/	**<0.001**
ppSS (700–1000)	[1] **Significance of Coefficient**	**<0.001**	/	**0.003**	**0.015**	**0.023**	/
	[1] **Standardized Coefficient**	0.45	/	−0.15	0.12	0.11	/
	[2] **Significance of Sectoral Effect**	**<0.001**	/	**0.005**	0.112	**0.029**	/
ASCOD– ppScleral	[1] **Significance of Coefficient**	**<0.001**	**0.039**	**<0.001**	**0.007**	/	**0.006**
	[1] **Standardized Coefficient**	0.38	0.10	−0.21	0.14	/	−0.15
	[2] **Significance of Sectoral Effect**	**0.015**	0.085	**<0.001**	**0.038**	/	**0.027**

[1] Associations between each global parameter and each variable are presented as a Standardized Coefficient and Significance as analyzed by multivariable linear regression.

[2] To assess if the effects of each variable varied by sector, a GEE model was employed on sectoral data *ppSS*: peripapillary scleral slope; *ASCOD–ppScleral*: ASCO depth relative to a peripapillary scleral reference plane; *ppCT*: peripapillary choroidal thickness; IOP: intraocular pressure.

Results are left blank for parameters not included in a given model for either global or sectoral effects analyses.